Ocean Engineering 118 (2016) 17–27

Contents lists available at ScienceDirect

Ocean Engineering

journal homepage: www.elsevier.com/locate/oceaneng

Development of vertical second harmonic wave loads of a large cruise ship in short and steep head waves

Satu K. Hänninen *,[1], Tommi Mikkola, Jerzy Matusiak

Aalto University, School of Engineering, Department of Applied Mechanics, P.O. Box 12200, FI-00076 Aalto, Finland

ARTICLE INFO

Article history:
Received 11 July 2015
Received in revised form
19 February 2016
Accepted 22 March 2016
Available online 6 April 2016

Keywords:
Springing excitation
Short waves
Second harmonic wave loads
RANS
Cruise ship
Hydrodynamics

ABSTRACT

The reliable prediction of springing excitation requires a detailed understanding of the origin of exciting wave loads. This study clarifies the origin of the second harmonic wave loads that can excite the springing of a large cruise ship (roughly 300 m long) in short and steep head waves. The findings are based on the analysis of previously validated numerical simulations (RANS-VOF) of the flow around a rigid hull. The accumulation of the loading is presented both along the length and the depth of the hull. The results show that the second harmonic vertical loading originates mainly in the foremost part of the ship, where the whole depth of the hull matters. The analysis focuses on the effect of the phase and the amplitude of second harmonic local loading. The irregular variation of the phase of the local loading with respect to that of the freely propagating wave demonstrates a serious deformation of the waves encountered in the area where the second harmonic total loading of the hull mainly originates. The analysis of the temporal behaviour of local loads indicates that the magnitude of the local second harmonic loading relates to the rise time of the respective local loads.

1. Introduction

Springing is a serious matter for ship builders and operators, because long-lasting vibration puts freighters at risk of fatigue damage and because it may affect the comfort of the passengers on a large cruise ship. The scientific community can help control the effects of springing by providing information on its origin and by providing tools that can predict springing in the design stage. A crucial question relating to the numerical prediction of springing is what the behaviour of the exciting wave loads is like from the hydrodynamic point of view. This study clarifies this matter by describing the development of the second harmonic wave loads that can cause springing (so-called second-order springing) in the case of a large cruise ship.

When searching for a numerical tool that can predict springing or another phenomenon, it is typical to conduct numerical simulations with a selected tool and to compare the numerical results against the corresponding experimental ones. Such comparisons provide information on the relevant physical phenomena, too. If the numerical and experimental results are similar, we can assume that the physics modelled by the numerical tool agree with the physics that matter for the phenomenon or vice versa. In the case of springing-type vibrations, the most authentic comparisons between the numerical and experimental results are the ones where the numerical simulations are compared against the vibratory response measured on board a full-scale ship. In such a case, the benchmark study of Storhaug et al. (2003) concluded that traditional seakeeping methods are not capable of predicting the springing response of a bulk carrier in realistic sea states. The methods that were tested in Storhaug et al. (2003) were different strip theories and one linear 3-D Rankine method. Soon afterwards, Vidic-Perunovic (2005) and Vidic-Perunovic and Jensen (2005) showed that the prediction of the springing response is improved when the effect of the bi-directional waves is included in a second-order strip theory. The capability of strip theories to predict springing is of interest from the point of view of practical design work, because strip theories require only scant computational resources in comparison to the other numerical tools: 3-D potential codes and Navier–Stokes solvers. From the point of view of physics, one challenge of strip theories is their limited capability to predict diffraction. For instance, Vidic-Perunovic (2010) pointed out the significance of the linear excitation caused by diffracted waves in the case of the springing of a container ship.

Overall, studying springing in the context of realistic sea states is a great challenge. The physics involved can be very complex for a ship advancing through irregular waves. Furthermore, the information on the prevailing sea state during the measurements may be vague, but it is needed as an input for the numerical simulations. The situation becomes more controlled and more

* Corresponding author.
E-mail address: satu.hanninen@iki.fi (S.K. Hänninen).
[1] Present address: Ship and Arctic Technology, VTT Technical Research Centre of Finland, P.O. Box 1000, FI-02044 VTT, Finland. Tel.: +358505770299.

http://dx.doi.org/10.1016/j.oceaneng.2016.03.052
0029-8018/

simplified when regular waves are studied by means of numerical simulations and model tests. When springing in regular waves is studied, the waves encountered are typically selected in such a way that linear wave loading or a multiple of the encounter frequency (ω_e) resonates with an eigenmode of the hull (ω_{hull}). This study focuses on the second harmonic wave loads ($2{\cdot}\omega_e = \omega_{hull}$), which can excite the springing of a large cruise ship. Springing excited by second harmonic wave loads is often called *second-order resonant springing* in the literature.

In the previous literature, second-order springing has been studied e.g. by comparing numerical and experimental results and by varying different case parameters such as the velocity of the ship and the height of the waves that are encountered. Kim et al. (2012), Lee et al. (2012), and Oberhagemann and el Moctar (2012), for instance, presented comparisons of the numerical and experimental results for a container ship using a Rankine panel method with a Timoshenko beam, a 3-D hydroelastic code with a 2-D beam model, and a RANS solver coupled with a model decomposition approach, respectively. They all report that the numerical results agree or are comparable with the experimental ones. From a theoretical point of view on hydrodynamics, the capability of a potential code to predict wave loads depends on the non-linear terms that are included in the model, while a RANS-VOF solver does not set any theoretical limitations on the non-linearity of the wave loads that can be predicted. The case parameters can matter for the significance of predicting different non-linear terms and for the requirements concerning the resolutions in RANS simulations. For instance, both an increase in the speed of the ship and an increase in the steepness of the waves encountered are reported to increase the second-order resonant springing. The effect of the speed of the ship has been demonstrated e.g. with experimental results in Storhaug and Moan (2007) and with numerical results in Shao and Faltinsen (2012). As for the wave height, the importance of the increasing wave height was demonstrated in the experimental studies of Slocum and Troesch (1983) and Miyake et al. (2008).

To conclude our overview of the existing knowledge on the matter of second-order resonant springing, the previous studies showed encouraging agreement between the numerical and experimental results and gave ideas about the significance of different case parameters. However, more detailed information on the development of second-order resonant springing is needed in order to understand the requirements for a tool that can predict exciting wave loads in the case of arbitrary case parameters. Such information is needed when selecting a tool for the reliable prediction of springing in realistic sea states as well.

This study describes what matters for the development of the second harmonic wave loads, which can excite the springing of a large cruise ship in one type of regular wave conditions. The findings are based on the analysis of the behaviour of the forces acting at stations on the ship. The data to be analysed was obtained by conducting numerical simulations with a RANS-VOF solver. The structural responses were omitted because of the low amplitude of vibration relating to the stiffness of cruise ships, which is greater than that of some other ship types.

The simulation results that form the basis of the analysis presented in this paper were verified and validated against experimental data in Hänninen et al. (2014) and in Hänninen (2014). The conclusions from these studies are that the numerical uncertainty is insignificant from the point of view of the present analysis and that in the selected case the modelling approach can capture the essential features of the development of the pressure impact at the bow. The validation was performed by comparing the computed time histories of the pressure at 10 locations against data which was obtained by conducting dedicated model tests. The numerical uncertainty of the computed pressure histories used in the validation is assessed in Hänninen et al. (2014) and in Hänninen (2014) by systematically studying the influence of grid and time resolution and the influence of the number of iterations within each time step. The verification of the time histories of the vertical forces acting at selected stations and the distribution of the second harmonic amplitude and phase of this force along the length of the hull is presented in Hänninen (2014). Additionally, the verification of the distributions of the first–third harmonic amplitude of the vertical forces acting at the stations for a similar computation is addressed in Hänninen et al. (2012). The requirements concerning the numerical simulation of a similar flow case are also considered in Hänninen and Mikkola (2008) and Hänninen et al. (2011). In this paper, the focus is on the physical phenomena only as the verification and the validation of the computation were done before.

2. Study case

The study case describes a large cruise ship that is advancing through short and steep head waves. The hull form is one of the development versions of a real ship which was constructed. The length of the ship is 328 m. The encounter period of the ship and waves was selected to be such that the second harmonic component of the wave loads resonates with the two-node vertical mode of the ship.

The computation is performed on the model scale 1:49. The ship frames are shown in Fig. 1 and the case parameters are presented in Table 1. The origin of the coordinate system is located at the aft perpendicular of the ship at the level of the design waterline. The positive z-axis points upwards and the positive x-axis from the stern towards the bow of the ship.

The setup applied in studying this case includes two assumptions about the physics of the flow. First, it is assumed that the motions of the ship are negligible, which implies that the effect of the radiation forces can be ignored. The validity of this assumption was confirmed by the measured data of the motions of the ship in the model tests (Hänninen et al., 2014; Hänninen, 2014). Second, it is assumed that the deformation of the hull (springing vibration) does not significantly affect the main features of the flow. As a consequence, the hull is considered rigid. The reasoning that underpins this assumption is that the order of magnitude of the vibration amplitude is about 1% of the wave height in this case.

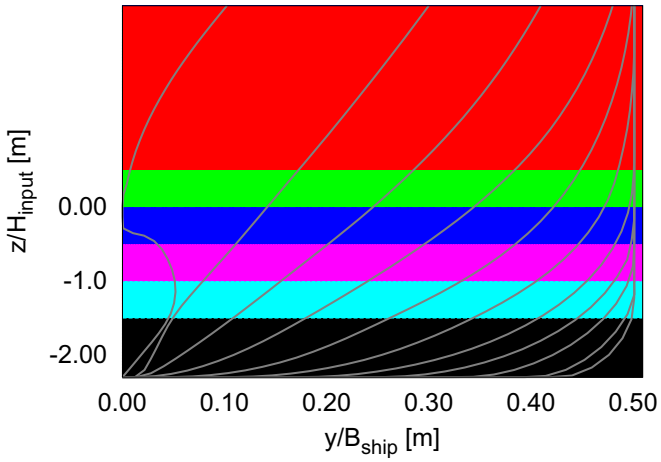

Fig. 1. Ship frames between the fore perpendicular and the midship. The colour zones are used in Section 5.2. (For interpretation of the colours in this figure, the reader is referred to the web version of this paper.)

Table 1
Ship and wave particulars on model scale. L_{ship} denotes the length between the perpendiculars of the ship. The draught is the draught at the velocity of the model (Hänninen et al., 2014; Hänninen, 2014).

Model scale	1:49		
Length L_{ship}	6.69 m	Wave length L_{wave}	1.05 m
Breadth B_{ship}	1.10 m	Wave height $H_{input} = 2A$	0.08 m
Draught	0.184 m	Wave steepness kA	0.24
Block coefficient	0.72	Encounter period t_e	0.38 s
Velocity V_{ship}	1.47 m/s		
Froude number	0.181		
Reynolds number	$0.982 \cdot 10^7$		

3. Numerical method

3.1. Mathematical model

The computation was performed using the ISIS-CFD flow solver, which is distributed by Numeca International under the name FINE™/Marine. The description of the governing equations follows Queutey and Visonneau (2007). The conservations of mass, momentum, and volume fraction are modelled with the equation of continuity, the Navier–Stokes equations, and the transport equation of the volume fraction in Eqs. (1)–(3), respectively. Eqs. (1)–(3) are written for incompressible fluids in a moving grid system. In the case of the equation of continuity, distinct phases are assumed to have constant densities. In the case of a moving grid, a so-called space conservation law is satisfied:

$$\int_S \vec{U}\cdot\vec{n}\, dS = 0, \tag{1}$$

$$\frac{\partial}{\partial t}\int_{V(t)} \rho\vec{U}\, dV + \int_{S(t)} \rho\vec{U}(\vec{U}-\vec{U}_d)\cdot\vec{n}\, dS = \int_{V(t)} \nabla\cdot\bar{T}\, dV - \int_{S(t)} p\vec{n}\, dS + \int_{V(t)} \rho\vec{g}\, dV, \tag{2}$$

$$\frac{\partial}{\partial t}\int_{V(t)} c_i\, dV + \int_{S(t)} c_i(\vec{U}-\vec{U}_d)\cdot\vec{n}\, dS = 0, \tag{3}$$

where V is the control volume and S its closed surface. The velocity of the surface is denoted with $\vec{U}_d$ and its outwards-directed unit normal vector with $\vec{n}$. $\vec{U}$ represents the velocity field, p the pressure field, $\bar{T}$ the stress tensor, $\vec{g}$ the gravity vector, and c_i the volume fraction of the fluid i.

The coupling of the velocity and pressure fields is performed with a SIMPLE algorithm that takes into account the presence of a density discontinuity; see Queutey and Visonneau (2007).

The behaviour of the free surface is modelled with the volume-of-fluid method, which predicts the flows of both the water and the air in the computational domain using Eq. (3). This means that $i=air$ or $i=water$. In each computational volume, the volume fraction c_i indicates the presence of fluid i ($c_i = 1$) or its absence ($c_i = 0$) or a mixture of the two fluids ($0 < c_i < 1$). The value $c_{air} = c_{water} = 1/2$ is selected as the free surface. Using these volume fractions, the fluid density ρ and the fluid viscosity μ are defined for each control volume with

$$\rho = c_{water}\cdot\rho_{water} + c_{air}\cdot\rho_{air}, \tag{4}$$

$$\mu = c_{water}\cdot\mu_{water} + c_{air}\cdot\mu_{air}, \tag{5}$$

respectively. In this case, the volume fraction c_{air} can be defined as $c_{air} = 1 - c_{water}$. Only the volume fraction c_{water} is solved from Eq. (3).

Table 2
Boundary conditions (Hänninen et al., 2014; Hänninen, 2014).

x_{min}	Far-field condition	x_{max}	Wave generator, first order Stokes
y_{min}	Mirror condition	y_{max}	Mirror condition
z_{min}	Prescribed pressure	z_{max}	Prescribed pressure
Deck	Slip wall	Hull	Wall with wall-functions

The turbulence model applied is Menter's STT $k-\omega$ model with wall functions.

The boundary conditions that were applied are given in Table 2. They are described below according to Numeca (2011). At the far-field boundary, the velocity is set to zero at the beginning of the computation. The variables that are imposed depend on the local flow direction with respect to the boundary patch. Depending on whether the flow enters or leaves the domain, a Dirichlet or a Neumann condition is applied. At the boundaries with the prescribed pressure, the pressure $p_{boundary}$ is set to the value

$$p_{boundary} = -\rho g\,(z_{boundary} - z_0), \tag{6}$$

where $z_{boundary}$ is the z-location of the boundary and z_0 the location of the free surface at the beginning of the computations. The fluid can both enter and exit at this boundary. At the boundary with the mirror condition, the geometry and the flow are assumed to be symmetric. Then the velocity field is assumed to be tangential to the mirror plane. At the boundary with the slip wall, the velocity component that is normal to the boundary is set to zero. Further, the turbulent production resulting from shear is neglected.

The wave generation at the boundary x_{max} is based on the first-order Stokes wave theory, which gives instantaneous wave height and velocity distribution at the boundary.

3.2. Setup for the flow solver

The discretisations of the governing equations are explained in Queutey and Visonneau (2007). In this study, second-order discretisation schemes were selected as user-defined options. In the case of the time derivatives, a second-order backward scheme is used; see Queutey and Visonneau (2007). In the case of the convective terms of momentum and turbulence equations, the GDS gamma differencing scheme is used; see Queutey and Visonneau (2007). In the case of the convective term of the volume fraction conservation equation, the BRICS blended reconstructed interface capturing scheme is used; see Wackers et al. (2011).

The computational domain includes only one half of the hull because of the symmetric flow case. The computational domain moves with the ship. The locations of the domain boundaries are given in Table 3; see also Fig. 2. The distance between the inlet boundary (x_{max}) and the bow is about three times the wave length, which gives the waves generated at the inlet enough distance to develop before reaching the bow. The distance between the stern and the outlet boundary (x_{min}) is such that the grid can be made coarse in front of the outlet boundary for wave damping without needing to make the grid coarse in the vicinity of the stern. No special treatment is applied at the outlet boundary for wave absorption. The locations of the lower boundary (z_{min}) and the upper boundary (z_{max}) are such that they do not affect the flow around the hull or the free propagation of the waves. The location of the

Table 3
Locations of the grid boundaries.

x_{min}/L_{wave}	−8.32	x_{max}/L_{wave}	9.23
y_{min}/L_{wave}	0.00	y_{max}/L_{wave}	6.63
z_{min}/L_{wave}	−8.13	z_{max}/L_{wave}	1.63

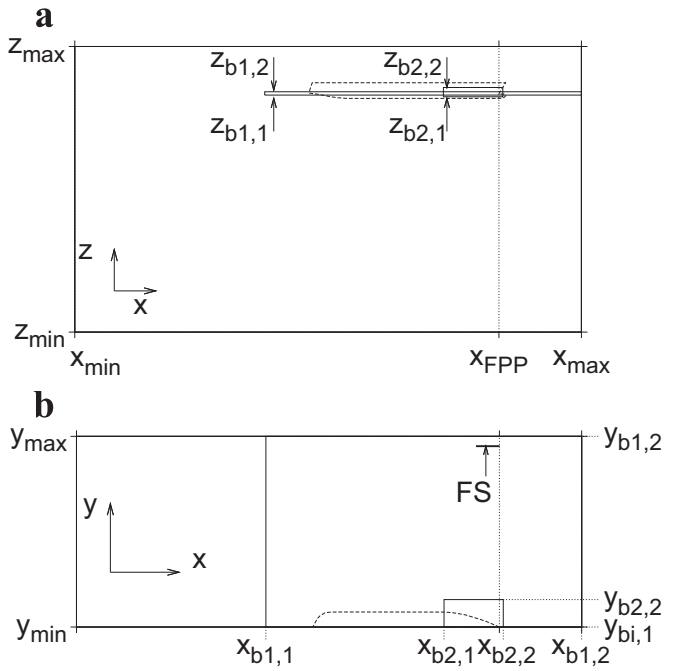

Fig. 2. Coordinate axes, boundaries of the computational domain (x_{min}, x_{max}, y_{min}, y_{max}, z_{min}, z_{max}), boundaries of the refinement boxes $b1$ and $b2$ ($x_{bi,1}$, $x_{bi,2}$, $y_{bi,1}$, $y_{bi,2}$, $z_{bi,1}$, $z_{bi,2}$), location of the fore perpendicular (x_{FPP}). The origin of the coordinate system is located at the aft perpendicular of the ship at the level of the design waterline: (a) xz-level, (b) xy-level; the line *FS* indicates the location of the analysis of the behaviour of the waves (Hänninen, 2014).

boundary y_{max} is such that the waves generated by the ship do not reflect from the boundary.

The spatial domain has three sub-domains of local refinements. One of them is designed for the transportation of waves in the computational domain (refinement box $b1$, Fig. 2, Table 5). This refinement box extends for the whole computational domain in the longitudinal and lateral directions, except in the vicinity of the outlet boundary (x_{min}), where the waves need to be dampened before they reach the outlet boundary. The vertical edges of this refinement box are such that the propagating waves fit into the box. Another local refinement (refinement box $b2$, Fig. 2, Table 5) is applied in the y-direction for capturing impact-type flow phenomena in the bow area of the ship. The edges of the refinement bow b_2 were selected according to the visual observations and pressure signals of the model tests of a similar flow case. The third local refinement covers the boundary layer near the hull surface.

Information on the resolution is given in Table 4. The number of cells, the cell height H_{cell} and length L_{cell} in the refinement boxes $b1$ and $b2$, and the first cell height y_1 in the boundary layer are given. The first cell height was selected to be such that the dimensionless distance from the wall y^+ gets the value of roughly 30 in the area of the stern of the ship. The stretching ratio in the boundary layer is 1.20. The grids were generated with the Hexpress hexahedral grid generator (version 2.11-1). The time step is given in Table 4. The number of iterations per time step was set to be 20, while the requirement for the decrease of the residuals (infinity norms) was set so high that practically it did not limit the iteration number; see Hänninen et al. (2014) and Hänninen (2014).

Table 4
Information on grids and time steps.

Number of cells	6.53M		
L_{wave}/L_{cell}	87.49	y_1	0.0013
H_{wave}/H_{cell}	11.94	$t_e/\Delta t$	367.86

Table 5
Locations of the boundaries of the refinement boxes $b1$ and $b2$ (Hänninen, 2014).

Location	$b1$	$b2$		$b1$	$b2$
$\lvert x_{FPP} - x_{bi,1}\rvert/L_{wave}$	8.12	1.93	$\lvert x_{FPP} - x_{bi,2}\rvert/L_{wave}$	2.86	0.13
$y_{bi,1}/L_{wave}$	0.00	0.00	$y_{bi,2}/L_{wave}$	6.63	0.95
$z_{bi,1}/L_{wave}$	−0.06	−0.12	$z_{bi,2}/L_{wave}$	0.06	0.21

Table 6
Information on fluids (Hänninen et al., 2014; Hänninen, 2014).

Water density ρ_{water}	998.1 kg/m^3	Air density ρ_{air}	1.2 kg/m^3
Water viscosity μ_{water}	0.001 kg/sm	Air viscosity μ_{air}	1.85×10^{-5} kg/sm
Standard gravity g	9.81 m/s^2		

At the beginning of the computation (0.00–3.00 s), the ship accelerates according to an acceleration ramp with the form 0.5–0.5 cos($t\pi$/ 3.00 s). The wave generation starts at the inlet boundary at the beginning of the simulation. The results to be analysed cover the time frame 6.98–10.80 s, which includes 10 encounter periods.

Table 6 gives information on the fluid properties in the computations.

The feasibility of the present setup for the computation is shown through a verification and validation study in Hänninen et al. (2014) and Hänninen (2014).

4. Analysis of the results

4.1. Forces

The focus is on the vertical force at the stations and on the vertical force that accumulates along the length of the hull.

The calculation of the vertical force $F_{z,station}$ at a station starts with the selection of the grid points that are located within a thin vertical section and represent the station (Hänninen et al., 2012). The points representing one half of the ship frame are organised in such a way that the point closest to the centreline of the ship is chosen to be the point $iy=1$, the second closest point is $iy=2$, and so forth. The bulb area is an exception. There, the points closest to each other are adjacent. The vertical force per unit ship length at a station is calculated using the trapezoidal rule:

$$F_{z,station}(t) = 2 \cdot \sum_{iy=2}^{N_{p,f}} \frac{1}{2} \cdot (p_{iy}(t) + p_{iy-1}(t)) \cdot (y_{iy} - y_{iy-1}), \tag{7}$$

where $N_{p,f}$ is the number of points that represent one half of the ship frame. In addition to the force $F_{z,station}$ acting on the whole frame, the force acting on a part of it has also been analysed. This can be evaluated using Eq. (7) by choosing points belonging to a specific part of the frame.

The total force acting on the hull can be calculated by adding up all the vertical forces at the stations multiplied by the width of the x-span that a frame force represents. The development of this total force along the length of the hull is called the cumulative force $F_{z,cum}$, which is defined between the stem of the ship and an x-location downstream using

$$F_{z,cum}(x, t) = \sum_{ix=1}^{n_{station}} F_{z,station,ix} \cdot dx, \tag{8}$$

where dx is the width of the x-span that a force at a station represents. The non-dimensional width of the x-span is $dx/L_{ship} = 0.0036$ in this study. The index $ix=1$ indicates the

foremost station and the index $ix = n_{station}$ indicates the rearmost station that is observed.

4.2. Discrete Fourier Transformation

The Discrete Fourier Transformation is applied when resolving the second harmonic component and low-pass filtered time histories of the forces and the phase of the freely propagating wave.

The second harmonic component is distinguished from the force history (after subtracting the mean value) by applying Discrete Fourier Transformation (DFT) e.g. Chapra and Canale (1988). The time history can be considered as a data sequence $F = F(n)$ of discrete times $n = 1, 2, \ldots, N_t$. The time step Δt affects the total number of points in the frequency domain through the Nyquist frequency $\pi/\Delta t$ and the length of the time history $L_t = N_t \Delta t$ defines the spacing of the frequency domain $\Delta\omega = 2\pi/L_t$.

The Fourier series of a real-valued time history F can be written as

$$F(n) = \sum_{k=1}^{N_\omega} a_k \cos\left(\frac{2\pi k}{N_t} n\right) + \sum_{k=1}^{N_\omega} b_k \sin\left(\frac{2\pi k}{N_t} n\right) \tag{9}$$

with

$$a_k = \frac{2}{N_t} \sum_{n=1}^{N_t} p(n) \cos\left(\frac{2\pi k}{N_t} n\right) \tag{10}$$

and

$$b_k = \frac{2}{N_t} \sum_{n=1}^{N_t} p(n) \sin\left(\frac{2\pi k}{N_t} n\right). \tag{11}$$

The second harmonic amplitude of the force is calculated in such a way that it includes the energy in the frequency span of width ω_e around the second harmonic encounter frequency:

$$\xi_{2,span} = \sqrt{\sum_{k=15}^{24} \left(a_k^2 + b_k^2\right)}. \tag{12}$$

As the length of the time histories is 10 times that of the encounter period, the index that corresponds to the second harmonic of the encounter frequency is 20 in the frequency domain. Hänninen (2014) and Hänninen et al. (2012) showed that the difference between the amplitude $\xi_{2,span}$ and the amplitude $\xi_{2,single} = \sqrt{(a_{20}^2 + b_{20}^2)}$ is negligible from a practical point of view. The definition that is applied in this study is more appropriate from the point of view of the springing excitation.

The phase of the second harmonic force at a station is calculated with

$$\delta_2 = \operatorname{atan}\left(\frac{b_{20,F_{z,station}}}{a_{20,F_{z,station}}}\right). \tag{13}$$

The distribution of the phase δ_2 of the second harmonic force $F_{z,station}$ is presented with the distribution of the phase δ_{wave} of the freely propagating waves. Here, δ_{wave} is the phase of the second harmonic component that is bounded to the freely propagating wave:

$$\delta_{wave} = 2 \cdot \operatorname{atan}\left(\frac{b_{10,wave}}{a_{10,wave}}\right). \tag{14}$$

The effect of the difference between the phases δ_2 and δ_{wave} on the cumulative force $F_{z,cum}$ is demonstrated by comparing the second harmonic amplitude of $F_{z,cum}$ (Eq. (8)) and the second harmonic amplitude of the cumulative force, which is calculated using the phase of the freely propagating wave as follows:

$$\xi_{2,span,F_{z,cum}(\delta_{wave})}(x) = \sum_{k=1}^{n_{station}} \xi_{2,span,F_{z,station,ix}} \cdot \cos(\delta_{wave,i} - \delta_{wave,1}) \cdot dx \tag{15}$$

In all, the cumulative force $F_{z,cum}$ depends on both the amplitude and the phase of the second harmonic force $F_{z,station}$ at a station. The joint effect of the amplitude and phase is presented by projecting the second harmonic amplitude of $F_{z,station}$ to the phase of the second harmonic total vertical force acting on the hull. The phase of the second harmonic total force is denoted as $\delta_{2,total}$. The projected second harmonic amplitude is calculated as

$$\xi_{2,proj} = \xi_{2,span}[\sin(\delta_2) \cdot \sin(\delta_{2,total}) + \cos(\delta_2) \cdot \cos(\delta_{2,total})]. \tag{16}$$

The low-pass filtered time histories, which consist either of the zeroth–first harmonic components or of the zeroth–second harmonic components are calculated with Eq. (9) using only the 14 and 24 lowest Fourier components, respectively.

4.3. Average time history and its rise time

The figures on time histories depict average time histories. The average time histories are the averages of the 10 encounter periods which the computational data includes. An instantaneous result of a quantity $\phi(t)$ is calculated with

$$\phi(t) = \frac{1}{10} \sum_{j=1}^{10} \phi_j(t), \tag{17}$$

where $\phi_j(t)$ is the corresponding instantaneous value of the jth encounter. The time histories for individual encounters are obtained by dividing the whole time history into 10 pieces whose length is one encounter period.

The rise time of a force history is calculated from the average time history with

$$t_{rise} = t_2 - t_1, \tag{18}$$

where t_1 is the instant when the average force history has its minimum value and t_2 is the instant when the average force history first reaches its maximum value after the instant t_1.

4.4. Non-dimensional results

All the results are presented in a non-dimensional form.

The time domain is made non-dimensional by division by the average of the encounter period t_e. An arbitrary instant is selected to be $t/t_e = 0.0$ and its value does not matter for the presentation of the results.

When the local pressures, the forces $F_{z,station}$, and the forces $F_{z,cum}$ are made non-dimensional, the average wave height H is used. H is calculated from the computational results between the x-location of the fore perpendicular and $x/L_{ship} = 0.88$ on the cross-section $y/B_{ship} = 6.0$. See Hänninen et al. (2014) and Hänninen (2014) for more details on H.

The local pressures p, the forces at the stations $F_{z,station}$, and the cumulative forces $F_{z,cum}$ are made non-dimensional as follows:

$$p^* = \frac{p}{\rho g H}, \quad F^*_{z,station} = \frac{2F_{z,station}}{\rho g B_{ship} H}, \quad \text{and} \quad F^*_{z,cum} = \frac{2F_{z,cum}}{\rho g L_{ship} B_{ship} H}, \tag{19}$$

respectively.

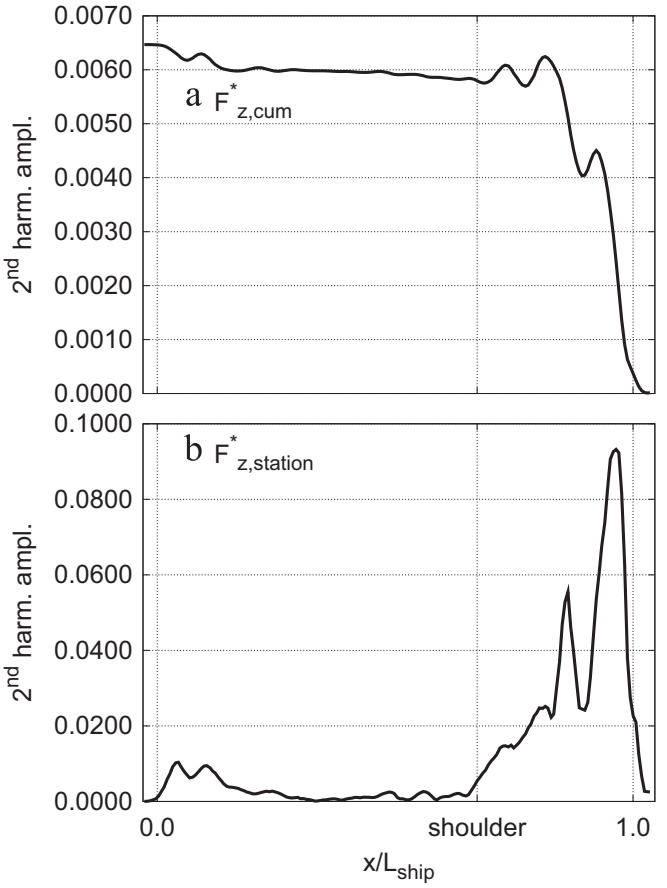

Fig. 3. Distributions of the second harmonic vertical loading for the whole length of the ship. (a) Cumulative force. (b) Amplitude of the force at the stations (Hänninen, 2014).

5. Development of the second harmonic loading along the hull surface

Sections 5.1 and 5.2 describe how different parts of the hull contribute to the total second harmonic loading in the longitudinal and vertical directions of the hull, respectively.

5.1. Development in the longitudinal direction of the hull

Fig. 3a shows how the second harmonic vertical force $F_{z,cum}$ accumulates along the length of the hull from the fore perpendicular to the aft perpendicular. The main contribution of the loading originates from the foremost part of the bow. For instance, within the distance of about $0.2L_{ship}$ from the fore perpendicular, the magnitude of the second harmonic vertical loading is roughly 94% of the respective loading of the whole ship. The accumulation of the second harmonic force $F_{z,cum}$ correlates with the second harmonic force $F_{z,station}$ acting at the stations. The essential increase of the cumulative force $F_{z,cum}$ (Fig. 3a) occurs in the same area where the amplitude of the second harmonic vertical force $F_{z,station}$ at the stations (Fig. 3b) is the largest. As the bow area makes the most significant contribution, it is observed in more detail below.

The accumulation of the second harmonic vertical force $F_{z,cum}$ is irregular in two ways: the rate of the increase and the decrease in the level of the force varies and the lengths of the x-spans of the increasing and decreasing force vary; see the black dotted line in Fig. 4a. The varying rate of the increase and decrease of the force $F_{z,cum}$ relates to the varying amplitude of the force $F_{z,station}$ at a station. The change in the cumulative force is high in the areas

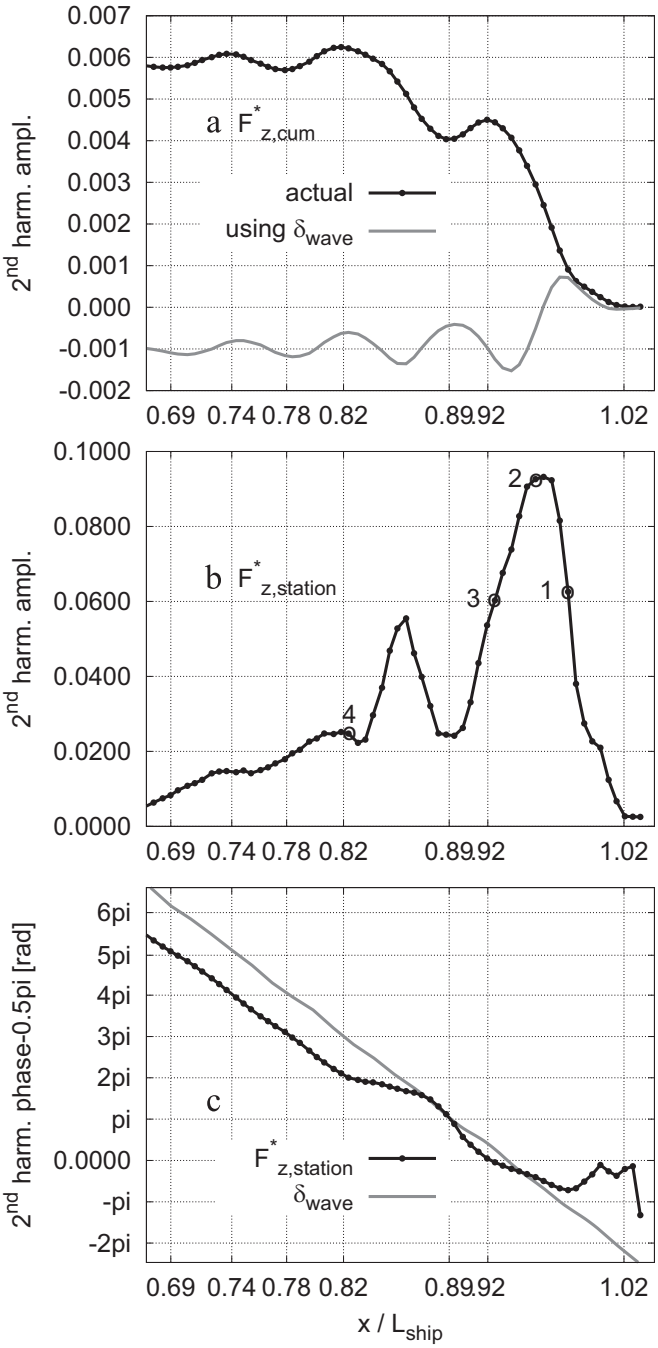

Fig. 4. Distributions of the second harmonic vertical loading in the area of the bow. (a) Amplitude of the cumulative force (actual) and amplitude of the cumulative force that is calculated using the phase of the wave. (b) Amplitude of the force at the stations; the numbers 1–4 indicate the locations at which the time histories of $F_{z,station}$ are studied in Section 6.1. (c) Phase of the forces at the stations $F^*_{z,station}$ in relation to the phase at $x/L_{ship} = 1.0$ and the phase of the freely propagating wave.

where the amplitude of the vertical force $F_{z,station}$ at a station is high, e.g. around $x/L_{ship} \approx 0.96$, and low in the areas where the amplitude of the vertical force $F_{z,station}$ at a station is low, e.g. around $x/L_{ship} \approx 0.74$; compare Fig. 4a and b. The varying lengths of the decreasing and increasing force relate to the distribution of the phase of the second harmonic force $F_{z,station}$ at stations; see the black dotted line in Fig. 4c. A local maximum or minimum of the cumulative force $F_{z,cum}$ (Fig. 4a) occurs when the phase shift of the forces $F_{z,station}$ at the stations (Fig. 4c) is roughly one π from the previous local minimum or maximum of the cumulative force $F_{z,cum}$ (Fig. 4a). In practice, the variation of the phase is irregular

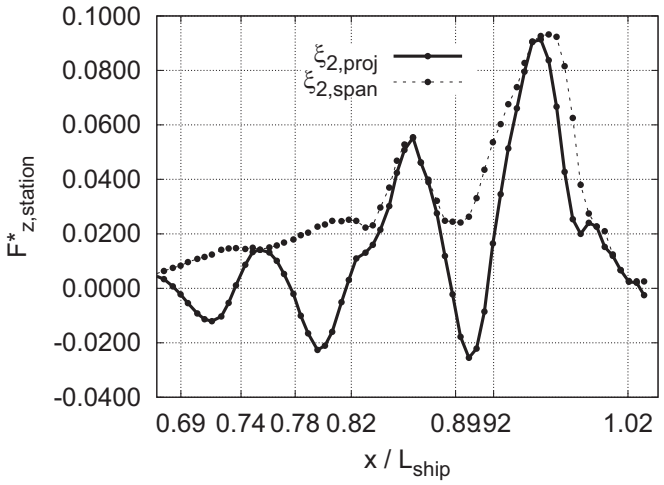

Fig. 5. Distributions of the second harmonic vertical loading in the area of the bow: the amplitude of the force at the stations and their projection to the phase of the total force.

forward of $x/L_{ship} \approx 0.82$, aft which it increases linearly. Aft $x/L_{ship} \approx 0.82$, the second harmonic phase has a fixed difference from the phase of the second harmonic component (δ_{wave}, Eq. 14) that is bounded to the freely propagating wave; see Fig. 4c. In the area where the phase difference between the force and the freely propagating wave is fixed ($x/L_{ship} < 0.82$), the variation of the amplitude of the cumulative force $F_{z,cum}$ continues but becomes smaller and smaller in the middle part of the hull, while its mean value does not change significantly; see Fig. 4a and also Fig. 3a. The effect of the irregular distribution of the phase of the second harmonic component of $F_{z,station}$ on the second harmonic amplitude of the cumulative force $F_{z,cum}$ can be seen by comparing the actual cumulative force and the cumulative force that is calculated using the phase of the freely propagating wave (Eq. (15)); see Fig. 4a. If the cumulative force was calculated using the phase of the freely propagating wave, the second harmonic amplitude of the loading of the whole ship would only be roughly 15 % of the actual loading.

In all, the accumulation of the force $F_{z,cum}$ relates both to the amplitude and to the phase of the second harmonic force $F_{z,station}$ at the stations. Their joint effect is illustrated in Fig. 5 by giving the second harmonic amplitude $\xi_{2,proj}$ of the force $F_{z,station}$, which is projected to the phase of the second harmonic total force; see Eq. (16). The force $F_{z,station}$ at a station makes the largest positive contribution to the accumulating force $F_{z,cum}$ when the force $F_{z,station}$ at the station is in the same phase as the total force and the largest negative contribution when the phase is opposite. This illustration gives slightly different locations for the zero contribution; in other words, the locations of the local minima and maxima of the accumulative force $F_{z,cum}$ are slightly different from those of the zero crossing of the projected force at the stations. The reason is that the phase of the accumulative force changes as a function of x.

5.2. Development in the vertical direction of the hull

This section describes how the loading at different depths of the hull contributes to the second harmonic force $F_{z,station}$ at the stations. In order to do this, the hull is divided into six horizontal parts limited by the deck, five waterlines, and the bottom of the ship; see Fig. 1.

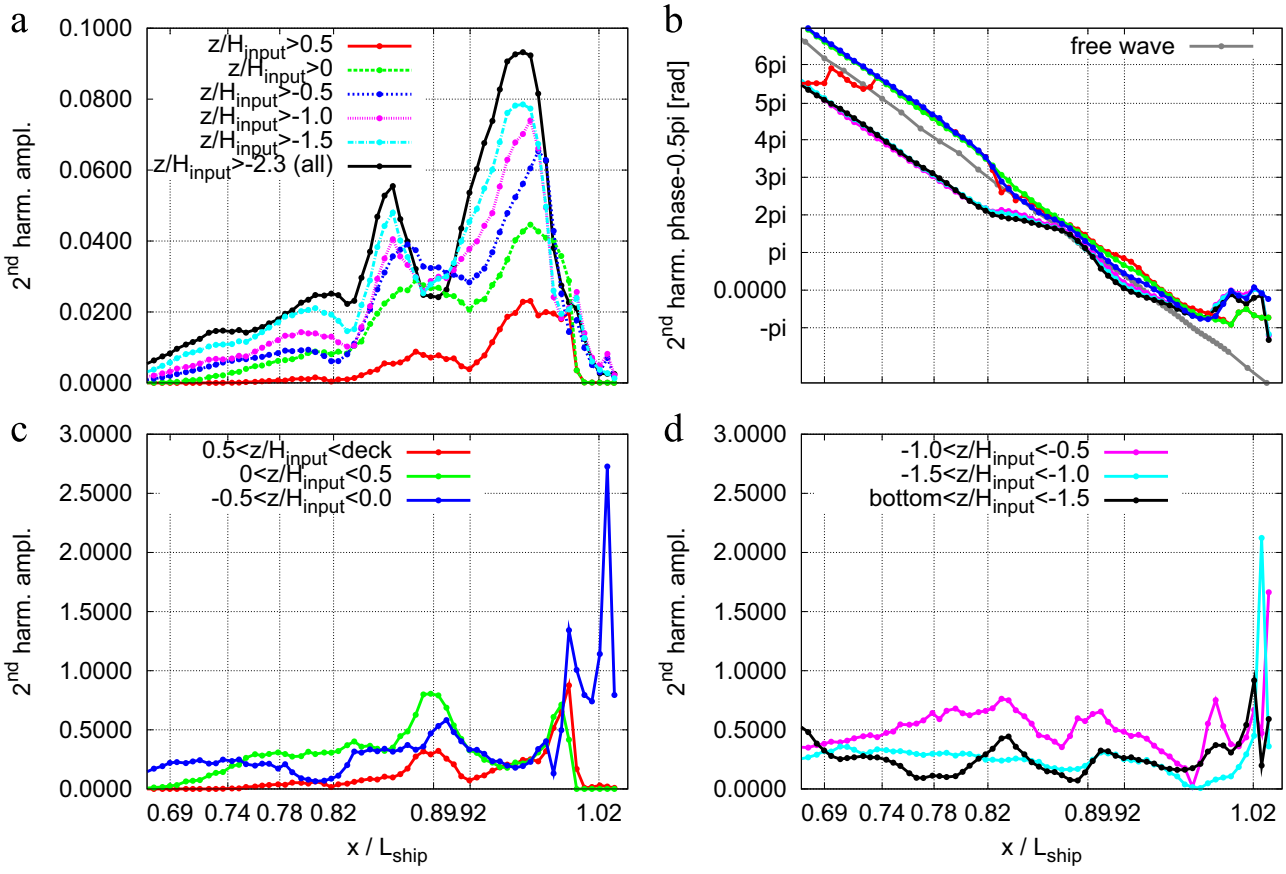

Fig. 6. (a) Accumulation of the second harmonic amplitude of $F_{z,station}$ when the area of observation is extended from the deck towards the bottom of the ship. (b) Phase of the second harmonic forces $F_{z,station}$ presented in Fig. 6a. (c) and (d) Second harmonic amplitude of the vertical force at stations acting in the horizontal stripes given in Fig. 1. (For interpretation of the colours in this figure, the reader is referred to the web version of this paper.)

Fig. 6a shows how the distribution of the second harmonic force $F_{z,station}$ at the stations accumulates towards its complete form when the area of the observation expands in the vertical direction from the deck towards the bottom of the hull. The significance of the loading at different depths varies along the length of the hull. Forward of the station $x/L_{ship} \approx 0.82$, the uppermost part of the hull $z/H_{input} > 0$ (the red and green lines in Fig. 6a) makes a particularly significant contribution (on average 57 %) to the total amplitude of the second harmonic force $F_{z,station}$. Nevertheless, all the horizontal parts of the hull matter for the total second harmonic amplitude of the forces $F_{z,station}$ and, thus, for the final shape of its distribution along the length of the hull. As an example, the bottom-most area of the hull $z/H_{input} < -1.5$ (the black line in Fig. 6a) contributes to the maximum value of the distribution ($x/L_{ship} \approx 0.96$) by 19 %. Aft the station $x/L_{ship} \approx 0.82$, all the horizontal parts of the hull below $z/H_{input} = 0.5$ (the green, blue, pink, turquoise, and black lines in Fig. 6a) contribute to the total amplitude of the frame forces $F_{z,station}$, while none of them has a particularly dominant effect.

When looking at the results in Fig. 6a, one should keep in mind that the change of the force $F_{z,station}$ as a result of the loading at a certain depth does not directly reflect the magnitude of the local loading at the respective depth. As a consequence of the phase differences between the local loadings at different depths of a station, the local loading at a certain depth can either increase or reduce the total loading at the station. Fig. 6b gives the distributions of the phase of the second harmonic forces $F_{z,station}$, whose amplitudes are presented in Fig. 6a. Forward of the station $x/L_{ship} \approx 0.82$, the differences between the distributions of the phase vary locally along the length of the hull. Both locations where the phase differences of the local loading have the most similar values ($x/L_{ship} \approx 0.97$ and $x/L_{ship} \approx 0.87$) occur in the area where the second harmonic amplitude of the force $F_{z,station}$ is increasing towards its maximum value. Aft the station $x/L_{ship} \approx 0.82$, the distributions of the phase are fixed in relation to each other. Thus, the phase difference between the loading at different depths does not cause variation in the distribution of the second harmonic amplitude of the force $F_{z,station}$ in that area.

Fig. 6c and d gives the second harmonic amplitude of the force $F_{z,station,str}$ acting at the previously mentioned horizontal stripes. The results in Fig. 6c and d are divided by the respective total force $F_{z,station,tot}$, which is shown as a black line in Fig. 6a. These results give different observations on the significance of the different depths for the loading in comparison with the results in Fig. 6a. For instance, the second harmonic force $F_{z,station,str}$ is the most significant on the horizontal stripes $-1.0 < z/H_{input} < -0.5$ (the pink line in Fig. 6d) and $-0.5 < z/H_{input} < 0.0$ (the blue line in Fig. 6c), the averages being $F_{z,station,str}/F_{z,station,tot} = 0.51$ and 0.37, respectively. These horizontal stripes do not make that significant a contribution to the accumulation of the second harmonic force $F_{z,station}$ in Fig. 6a (the pink and blue lines) because of the phase difference from the loading in the upper parts of the hull (the green and red lines in Fig. 6a). The comparison of the magnitude of the forces within the horizontal stripes in Fig. 6c and d and the accumulation of the total force $F_{z,station}$ in Fig. 6a underlines the fact that the phase difference between the loading at different depths of the hull makes the total second harmonic amplitude of the force $F_{z,station}$ smaller than the sum of the local forces $F_{z,station,str}$ would be.

6. Second harmonic component and the temporal behaviour of the loading

Section 6.1 describes how the effect of the second harmonic loading is seen in the temporal behaviour of the forces acting at the stations in the present study case. Section 6.2 presents a theoretical analysis that supports the findings of Section 6.1.

6.1. Identifying the second harmonic loading in the temporal behaviour of the forces at the stations

This section describes how the development of the second harmonic amplitude of the force $F_{z,station}$ at the stations along the length of the hull is seen in the temporal behaviour of the forces. First, four force histories are presented as examples; the locations of these stations are indicated by the numbers 1–4 in Fig. 4b. Second, the temporal behaviour of the force $F_{z,station}$ is commented on for the whole area under observation in Fig. 4b.

Immediately aft the fore perpendicular at $x/L_{ship} = 0.98$ (Number 1 in Fig. 4b), the second harmonic amplitude of $F_{z,station}$ is increasing towards its maximum value. The respective unfiltered force history (the black line in Fig. 7a) shows distinctly impact-type behaviour with a sudden rise at $t/t_e \approx 0.1$. The total rise time is $t_{rise}/t_e = 0.22$, as defined by Eq. (18). The comparison of the low-passed filtered time history with the zeroth–second harmonic components (the red line) and the unfiltered time history (the black line) shows that the most distinct features of the impact relate to the third–*n*th harmonic components of the force. The comparison of the low-passed filtered time histories with the zeroth–second harmonic components and with the zeroth–first harmonic components (the red and green lines) shows that the second harmonic component correlates with the asymmetric behaviour of the force history.

Aft $x/L_{ship} = 0.98$, the second harmonic amplitude increases until it reaches its maximum value in the vicinity of $x/L_{ship} = 0.96$ (Number 2 in Fig. 4b). The unfiltered time history at $x/L_{ship} = 0.96$ (the black line in Fig. 7b) behaves more smoothly than the one at $x/L_{ship} = 0.98$. The rise time (Eq. (18)) is somewhat longer ($t_{rise}/t_e = 0.28$). The force history can be presented quite accurately with the zeroth–second harmonic components only; compare the black and red lines in Fig. 7b. The comparison of the low-pass filtered time histories with the zeroth–second and zeroth–first harmonic components (the red and green lines in Fig. 7b) shows that again the contribution of the second harmonic component correlates with the asymmetric behaviour of the force history.

Aft $x/L_{ship} = 0.96$, the second harmonic amplitude mainly decreases (Fig. 4b). The force histories at the stations $x/L_{ship} = 0.93$ and $x/L_{ship} = 0.82$ make it possible to observe what happens when the second harmonic amplitude decreases gradually. The asymmetry of the force history decreases. Fig. 7c and d shows that the difference between the low-pass filtered time histories with the zeroth–second harmonic and the zeroth–first harmonic components become smaller and smaller further from the fore perpendicular. At $x/L_{ship} = 0.93$, the second harmonic amplitude has a similar value as at $x/L_{ship} = 0.98$, but now the rise time is significantly longer, being $t_{rise}/t_e = 0.37$. At $x/L_{ship} = 0.82$, the second harmonic amplitude is already minor. The force history is symmetric in practice, the rise time being $t_{rise}/t_e = 0.47$.

In all, the magnitude of the second harmonic component correlates with the asymmetry of the force history in this study case. A parameter that can describe the asymmetry is the rise time of the force history. Fig. 8 compares the distribution of the rise time t_{rise}/t_e of the force $F_{z,station}$ at a station to the distribution of the second harmonic component of the force $F_{z,station}$; see the black and grey lines in Fig. 8, respectively. This comparison indicates that there is a correlation between the distribution of the second harmonic amplitude of the force and its rise time t_{rise}. The red line in Fig. 8 shows the rise time t_{rise}/t_e of the low-pass filtered time history with the zeroth–second harmonic components. The two distributions of the rise time are rather similar. Naturally, the difference between them is greatest aft the stem, where the force histories include a significant contribution of the third–*n*th harmonic components.

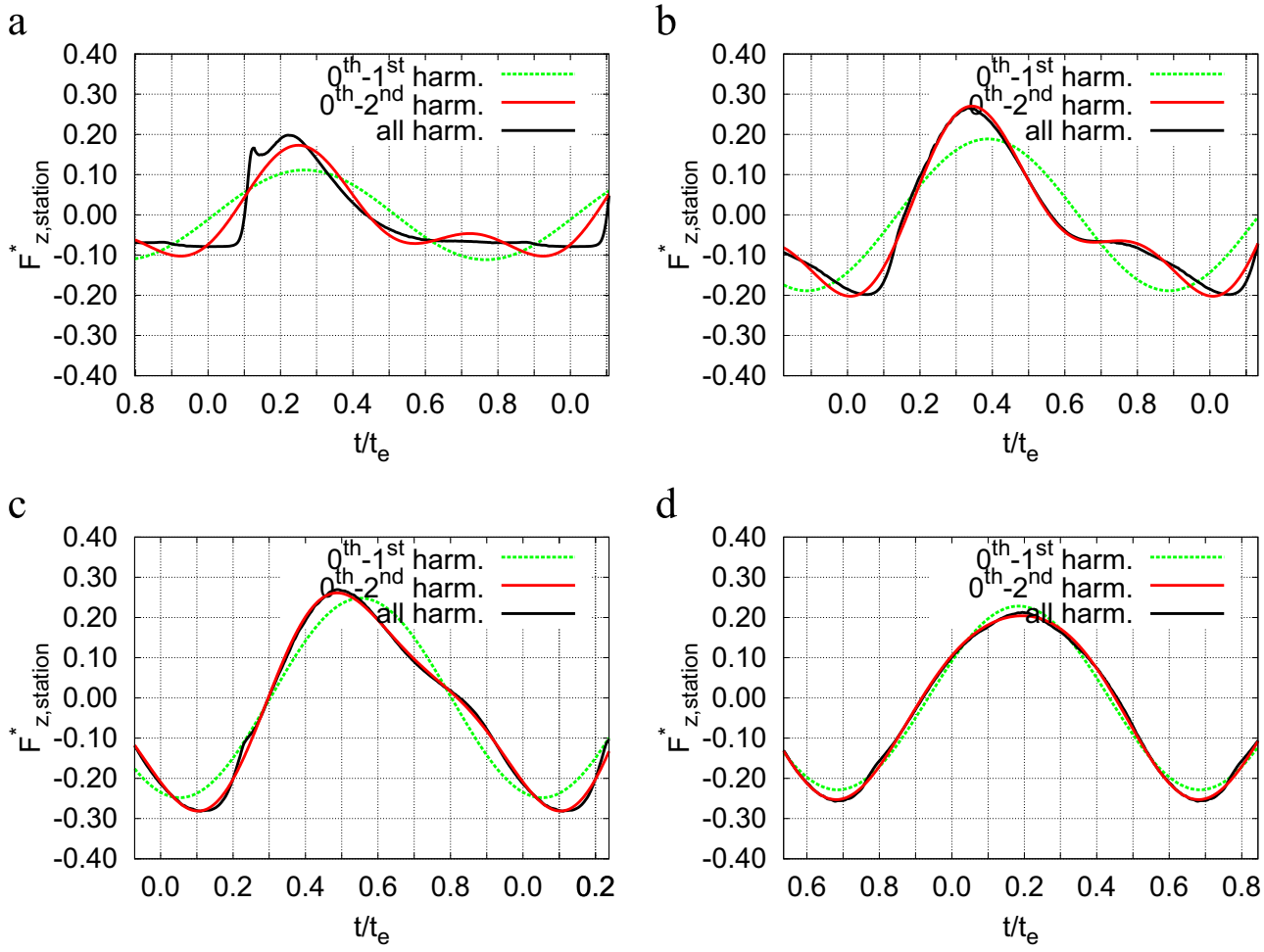

Fig. 7. Unfiltered vertical force (all harm.), low-pass filtered vertical force histories with the zeroth–second and zeroth–first harmonic components. (a) $x/L_{ship} = 0.98$, (b) $x/L_{ship} = 0.96$, (c) $x/L_{ship} = 0.93$, and (d) $x/L_{ship} = 0.82$. (For interpretation of the colours in this figure, the reader is referred to the web version of this paper.)

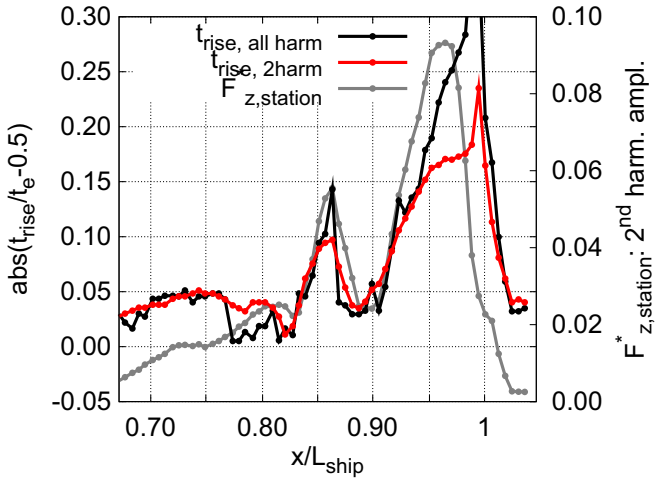

Fig. 8. Distributions of the rise time t_{rise}/t_e and the second harmonic amplitude of the vertical force at the station $F^*_{z,station}$. (For interpretation of the colours in this figure, the reader is referred to the web version of this paper.)

6.2. On the correlation between the second harmonic amplitude and the rise time of a time history

This section addresses further the relation of the second harmonic component of the force history and the rise time of the low-passed filtered force history with the zeroth–second harmonic components in order to confirm that a correlation between the rise time and the second harmonic component exists.

Let us first consider the rise time of an arbitrary time history $y(t)$, which consists of first and second harmonic components:

$$y(t) = C_1 \sin(\omega t + \delta_1) + C_2 \sin(2\omega t + \delta_2), \tag{20}$$

where $C_k = \sqrt{a_k^2 + b_k^2}$ with a_k and b_k defined in Eqs. (10) and (11), respectively, $\omega_k = 2\pi k/L_t$, and δ_k a phase. The rise time t_{rise} of the time history $y(t)$ can be expressed using two parameters: the ratio of the second and first harmonic amplitudes C_2/C_1 and the phase difference $\delta_2 - \delta_1$ between the components. The lines in Fig. 9a show $|t_{rise}/t_e - 0.5|$ as a function of the amplitude ratio C_2/C_1. When $C_2/C_1 > 0.4$, $|t_{rise}/t_e - 0.5|$ depends nearly unambiguously on C_2/C_1. When $C_2/C_1 < 0.4$, $|t_{rise}/t_e - 0.5|$ also depends on the phase difference. However, when the phase difference $(\delta_2 - \delta_1)/2\pi$ is not close to the values zero, 0.5, and one, $|t_{rise}/t_e - 0.5|$ depends nearly unambiguously on the amplitude ratio C_2/C_1 even if $C_2/C_1 < 0.4$; see the red lines in Fig. 9a.

The black dots in Fig. 9a show the respective results for the low-pass filtered time histories of the forces $F_{z,station}$ with the zeroth–second harmonic components in the bow area of the ship. Most of the results have a nearly unambiguous correlation between $|t_{rise}/t_e - 0.5|$ and C_2/C_1. The red dots in Fig. 9b show how the results with a nearly unambiguous correlation are distributed along the length of the bow area of the ship. The only areas where the correlation is not unambiguous are at $0.77 \le x/L_{ship} \le 0.83$ and

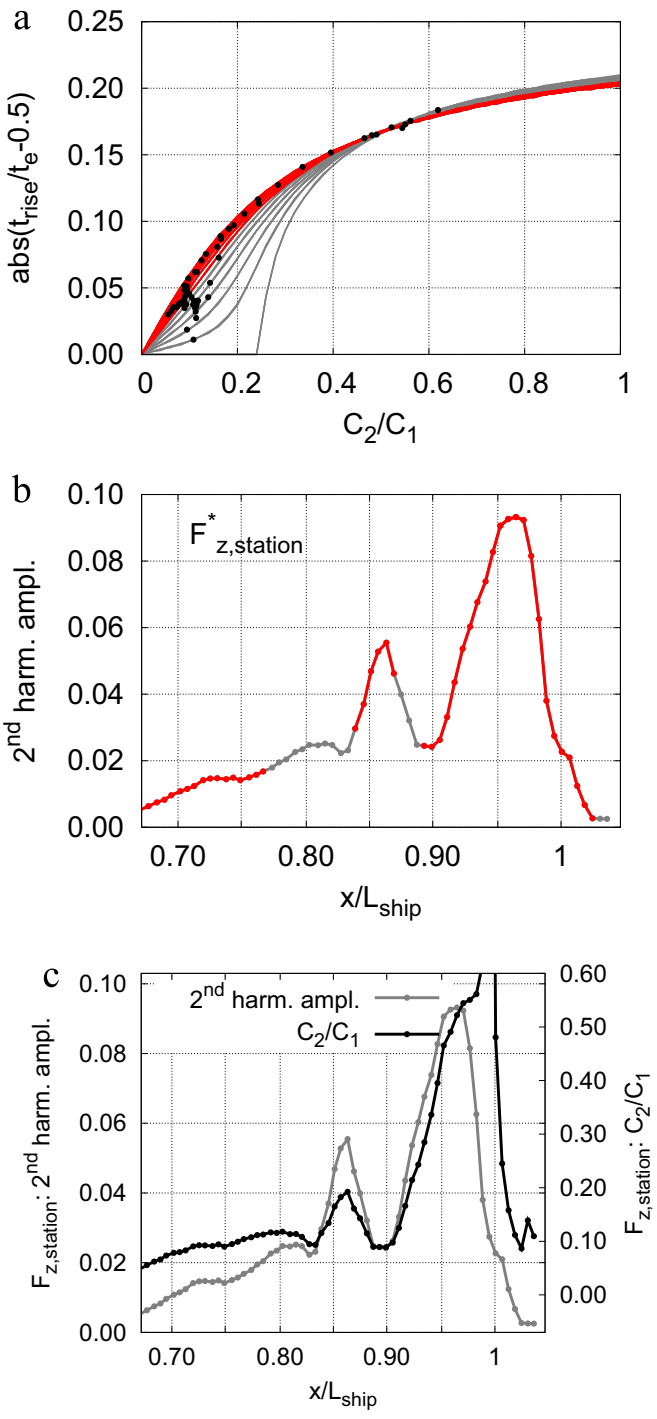

Fig. 9. (a) The lines represent the analytical solution of Eq. (20) with different values of the phase difference and the black dots the results of the present study case. The red lines indicate that the phase difference $(\delta_2 - \delta_1)/2\pi$ is different from the values 0, 0.5, and 1. (b) The distribution of the second harmonic amplitude of $F^*_{z,station}$: the colour red indicates that the correlation between C_2/C_1 and t_{rise}/t_e is nearly unambiguous. (c) Distributions of the second harmonic amplitude and amplitude ratio C_2/C_1 of $F_{z,station}$. (For interpretation of the colours in this figure, the reader is referred to the web version of this paper.)

$0.87 \leq x/L_{ship} \leq 0.89$; see the grey dotted line in Fig. 9b. Moreover, in the area $0.82 < x/L_{ship} < 1$, the rise time gets values $0 < t_{rise/t_e} < 0.5$. This implies that the rise time t_{rise}/t_e can be used as an indicator of the amplitude ratio C_2/C_1 of the low-pass filtered time history of $F_{z,station}$ with the zeroth–second harmonic components in the area where the most significant loading exists.

These findings support the observation in Section 6.1 according to which the rise time and the second harmonic amplitude of $F_{z,station}$ correlate. However, caution is needed when a time history includes third–nth harmonic components. In addition, the variation of the first harmonic amplitude in the area under observation should be taken into account. Fig. 9c shows that the distributions of the second harmonic amplitude of $F_{z,station}$ and of the ratio C_2/C_1 are rather similar in this case, even if some differences exist.

7. Discussion and conclusions

On the whole, the findings of this study underline that the development of the second harmonic wave loads, which can excite the springing of a large cruise ship, is a complex phenomenon. The results show that the accumulation of the excitation along the length of the hull can be explained on the basis of the variation of both the phase and the amplitude of the second harmonic force acting at the stations.

In the foremost part of the ship, where the excitation mainly originates, the distribution of the phase of the second harmonic vertical force at the stations is irregular and does not follow the phase of the freely propagating wave. Moreover, the phase of the loading at the individual stations varies as a function of depth in an irregular manner between different stations. These findings indicate that the hull has a significant effect on the propagation of the wave in the vicinity of the hull in the foremost part of the ship. In other words, the three-dimensional effects of the flow play an important role in the loading in that area. Moreover, this study shows that, aft the foremost part of the ship in the vicinity of the fore shoulder, the phase difference between the second harmonic vertical force at stations at different depths and the freely propagating wave becomes fixed. Simultaneously, the second harmonic amplitude of the vertical force at the stations starts decreasing. These observations imply that the effect of the hull on the flow and the magnitude of the local loading decrease simultaneously. The present findings on springing-type excitation are in line with the previous studies that suggest that the diffraction matters for springing, e.g. Vidic-Perunovic (2010), and with the studies that demonstrate that 3D methods with sufficient non-linear terms are capable of predicting springing, e.g. Kim et al. (2012), Lee et al. (2012), and Oberhagemann and el Moctar (2012), and with the studies that report that strip methods fail to predict springing, e.g. Storhaug et al. (2003).

The present results demonstrate that the second harmonic amplitude of the vertical force at a station and the accumulation of the total force are at their largest in the foremost part of the ship. This is a logical finding as the bow encounters the head waves first. It is more surprising that the present results show that the whole depth of the hull matters for the accumulation of these amplitudes. Furthermore, it is worth noticing that the actual magnitude of the local loading at a certain depth cannot necessarily be seen when studying the accumulation of the force in the vertical direction, because the loadings at different depths can cancel each other out as a result of the phase difference.

As for the variation of the second harmonic amplitude of the force at the stations along the length of the hull, this study shows that the ratio of the second and first harmonic amplitude correlates with the rise time of the force at the station. Basically, the rise time of the force must be distinctly shorter than the fall time or vice versa in order for there to be a significant second harmonic force. In this case, the rise time is distinctly shorter than the fall time at the locations where the second harmonic component loading is significant. This can mean impact-type behaviour of the loading, which typically becomes more important at higher ship speeds and when the height of the waves that are encountered is greater. Previous studies have shown that such matters make the

second-order resonant springing more important; see e.g. Storhaug and Moan (2007), Shao and Faltinsen (2012), Slocum and Troesch (1983), and Miyake et al. (2008). All in all, showing a correlation between the second harmonic amplitude and the rise time of the force is important, because it allows the accumulation of the springing excitation to be connected to local and temporal flow phenomena in future work.

To conclude, this study indicates that correct prediction of the second-order resonant springing excitation can require careful prediction of the variation of both the phase and amplitude along the length of the hull. This means that the effect of the hull on the propagation of the waves that are encountered must be predicted in detail and that the variation of the rise time of loading between different stations must be captured. In practice, this study indicates that the numerical tools that are used to predict springing should model the three-dimensional and impact-type behaviour of the flow.

Acknowledgements

This study was mainly carried out within a research project funded by the Academy of Finland. In addition, the first author got financial support for writing the paper from Aalto University School of Engineering and VTT Technical Research Centre of Finland. The financial support is gratefully acknowledged. The computational resources provided by CSC – the Finnish IT Center for Science – are also gratefully acknowledged.

References

Chapra, S.C., Canale, R.P., 1988. Numerical Methods for Engineers, 2nd edition. McGraw-Hill, Inc., Singapore.

Hänninen, S.K., 2014. Second Harmonic Wave Loads as Springing Excitation of a Large Cruise Ship in Short and Steep Head Waves (Doctoral thesis), Department of Applied Mechanics, School of Engineering, Aalto University, ⟨http://urn.fi/URN:ISBN:978-952-60-5671-5⟩.

Hänninen, S.K., Mikkola, T., 2008. Wave excitation on a ship bow in short waves. In: 14th Numerical Towing Tank Symposium, Poole, England.

Hänninen, S.K., Mikkola, T., Matusiak, J., 2011. Comparing computed and measured ship wave load distribution. In: 14th Numerical Towing Tank Symposium, Poole, England.

Hänninen, S.K., Mikkola, T., Matusiak, J., 2012. On the numerical accuracy of the wave load distribution on a ship advancing in short and steep waves. J. Mar. Sci. Technol. 17 (2), 125–138.

Hänninen, S.K., Mikkola, T., Matusiak, J., 2014. Computational and experimental study on local ship loads in short and steep waves. J. Mar. Sci. Technol. 19 (1), 103–115.

Kim, J.-H., Kim, Y., Kang, B.-C., Kim, Y., 2012. Ship springing analysis for very large container ship. Int. J. Offshore Polar Eng. 22 (3), 217–224.

Lee, Y., White, N., Wang, Z., Zhang, S., Hirdaris, S., 2012. Comparison of springing and whipping responses of model tests with predicted nonlinear hydroelastic analyses. Int. J. Offshore Polar Eng. 22 (3), 209–216.

Miyake, R., Matsumoto, T., Zhu, T., Abe, N., 2008. Experimental studies on the hydroelastic response due to springing using a flexible mega-container ship model. In: 8th International Conference on HydroDynamics, Nantes, France.

Numeca, 2011. User manual FINE™/Marine v2.3, Documentation v2.3b.

Oberhagemann, J., el Moctar, O., 2012. Numerical and experimental investigations of whipping and springing of ship structures. Int. J. Offshore Polar Eng. 22 (2), 108–114.

Queutey, P., Visonneau, M., 2007. An interface capturing method for free-surface hydrodynamic flows. Comput. Fluids 36, 1481–1510.

Shao, Y.-L., Faltinsen, O.M., 2012. A numerical study of the second-order wave excitation of ship springing in infinite water depth. In: Proceedings of the Institution of Mechanical Engineers, Part M: Journal of Engineering for the Maritime Environment, vol. 226, no. 2, pp. 103–119.

Slocum, S., Troesch, A.W., 1983. Non-Linear Ship Springing Experiments. Technical Report 226, Department of Naval Architecture and Marine Engineering, College of Engineering, The University of Michigan.

Storhaug, G., Moan, T., 2007. Springing/whipping response of a large ocean-going vessel—investigated by an experimental method. In: 10th International Symposium on Practical Design of Ships and Other Floating Structures, Houston, Texas, United States of America.

Storhaug, G., Vidic-Perunovic, J., Rüdinger, F., Holtsmark, G., Helmers, J.B., Gu, X., 2003. Springing/whipping response of a large ocean going vessel—a comparison between numerical simulations and full-scale measurements. In: 3rd International Conference on Hydroelasticity in Marine Technology, Oxford, UK.

Vidic-Perunovic, J., 2005. Springing Response due to Bidirectional Wave Excitation (Ph.D. thesis), Department of Mechanical Engineering, Technical University of Denmark.

Vidic-Perunovic, J., 2010. Towards the prediction of hull springing response. In: ASME 2010, 29th International Conference on Ocean, Offshore and Arctic Engineering, OMAE2010, Shanghai, China.

Vidic-Perunovic, J., Jensen, J.J., 2005. Non-linear springing excitation due to a bidirectional wave field. Mar. Struct. 18, 332–358.

Wackers, J., Koren, B., Raven, H.C., van der Ploeg, A., Starke, A.R., Deng, G.B., Queutey, P., Visonneau, M., Hino, T., Ohashi, K., 2011. Free-surface viscous flow solution methods for ship hydrodynamics. Arch. Comput. Methods Eng. 18, 1–41.